Springer

Acta Mechanica Sinica

CrossMark click for updates

• RESEARCH PAPER •

Acta Mech. Sin., Vol. 39, 323064 (2023)
https://doi.org/10.1007/s10409-023-23064-x

Vortex-induced energy loss of a mixed-flow waterjet pump under different operating conditions

Kan Kan[1,2], Yuhang Xu[1], Hui Xu[2,3], Jiangang Feng[3], and Zixuan Yang[4*]

[1] *College of Energy and Electrical Engineering, Hohai University, Nanjing 211100, China;*
[2] *College of Water Conservancy and Hydropower Engineering, Hohai University, Nanjing 210098, China;*
[3] *College of Agricultural Science and Engineering, Hohai University, Nanjing 210098, China;*
[4] *Institute of Mechanics, Chinese Academy of Sciences, Beijing 100190, China*

Received February 10, 2023; accepted March 20, 2023; published online May 23, 2023

Mixed-flow waterjet pumps (M-FWPs) are core units of high-speed ship power propulsion. When operated under non-optimal operating conditions, the unstable flow generated in the flow passage leads to a reduction in pump efficiency. This article investigates the energy loss mechanism of M-FWPs under different operating conditions through entropy production theory based on numerical simulations. The analyses of the simulation data show that the turbulence dissipation (EPTD) makes the dominant contribution to the entropy production rate. By comparing the correlations of velocity gradient, vorticity, and turbulent kinetic energy (TKE) with the EPTD, it is discovered that under non-optimal operating conditions, the inflow angle at the impeller inlet does not match the blade inlet angle at the leading edge of the blade, resulting in unsteady flow structures such as flow separation and large-scale vortices. The increase in vorticity and TKE caused by these unsteady structures ultimately causes the generation of turbulent entropy. Further examination of the enstrophy transport equation indicates that the relative vortex generation term plays a dominant role in the development of the unsteady flow in the flow passage.

Mixed-flow waterjet pump, Entropy production, Turbulence dissipation, Enstrophy transport

Citation: K. Kan, Y. Xu, H. Xu, J. Feng, and Z. Yang, Vortex-induced energy loss of a mixed-flow waterjet pump under different operating conditions, Acta Mech. Sin. **39**, 323064 (2023), https://doi.org/10.1007/s10409-023-23064-x

1. Introduction

Water jet propulsion is an advanced technology used in military ships. Compared to other propulsion approaches, it shows advantages in three aspects. First, water jet propulsion shows good anti-cavitation performance at high speeds and its sound pressure level in water is relatively low in comparison with propeller propulsion. Furthermore, installed in a flow passage with well-designed geometry, the pump operates smoothly, and as such the hull vibration and impeller operational damage can be reasonably reduced. Finally, water jet propulsion shows strong adaptability in fully utilizing power system efficiency in response to sudden changes in operation conditions. This feature helps extend the service life of ships with complex operation conditions. Due to these advantages, mixed-flow waterjet pumps (M-FWPs) are equipped on many high-speed and high-performance ships [1,2].

Despite the advantages of M-FWPs, certain issues remain in the operation process. In particular, when it is in operation, flow separation and large-scale vortices are generated in the flow passages of the pump, which tend to reduce the application value of the M-FWP. In this regard, it is useful to study the energy loss generation mechanism of M-FWP and its relation to flow structures.

Experiments and numerical simulations are currently the dominant research approaches of fluid dynamics [3-5]. Among the experimental studies on M-FWPs, the particle image velocimetry (PIV) technique is used by Wu et al. [6-8] to investigate the mechanism of flow structure formation and the associated flow field characteristics within the flow

*Corresponding author. E-mail address: yangzx@imech.ac.cn (Zixuan Yang)
Executive Editor: Lihao Zhao

passages of the pump. It is found that the tip leakage vortices (TLV) generated at the tip of the blade suction side (BSS) are directed towards the adjacent blade pressure surface (BPS). Miorini et al. [9] claimed that the TLV generation and development mechanism lead to changes in the characteristics of flow within the flow passage. Compared to laboratory experiments, numerical simulations show advantages in terms of acquiring flow field data at an arbitrary location along the flow passage. Through numerical simulations, Guo et al. [10] found that TLV generation and associated cavitation suppressed the leakage flow at the blade tip. They also pointed out that both TLV and cavitation can amplify the pressure pulsation, particularly in the tip region. Huang et al. [11,12] found that the cavitation enhanced the vorticity generation within the M-FWP, and served as an important mechanism for boundary vorticity diffusion. By analyzing the vorticity transport equation, they further pointed out that the vortex stretching term was the main trigger for the formation of large-scale vortices. Cao et al. [13] investigated the effect of inflow conditions, and discovered that the non-uniformity of the suction vortices led to a significant pressure drop in the pump.

The aforementioned investigations mainly focused on dynamics of the TLV and the associated cavitation formation and development mechanisms. However, studies on the energy loss mechanism within the M-FWPs are lacking. In the present study, numerical simulations are performed to investigate the energy loss properties of M-FWP.

In the literature, the differential pressure method is utilized extensively to evaluate the energy losses of hydraulic machines. This method can calculate the integral hydraulic losses of the pump, but is unable to identify the location where the energy losses take place. From the point of view of the second law of thermodynamics, the production of energy loss is a process of entropy increase. By analyzing the production of entropy, the energy loss in a specific area can be evaluated. Herwig et al. [14] verified the entropy production theory using experimental data of laminar and turbulent channel flows. Guan et al. [15] used the entropy production method to analyze the efficiency of the guide vane pair model and performed the hydraulic optimization of a centrifugal pump. Yang et al. [16] studied a high-speed pump and concluded that the hydraulic losses were mainly caused by turbulence dissipation around the impeller and guide vanes.

While many studies have already been conducted to investigate the internal flow energy losses in a variety of hydraulic machineries, the investigations of the energy losses of M-FWPs are lacking in the literature. Against this background, we investigate the composition of the energy losses within the M-FWP based on the entropy production method under different flow-rate operation conditions. The correlations of velocity gradient, vorticity, turbulence intensity, and turbulence dissipation with energy loss are also analyzed. Finally, the enstrophy transport equation is studied to reveal the relationship between the spatial evolution of vortices and energy loss.

The remainder of this paper is organized as follows: The numerical method, entropy production theory, and geometric characteristics of the M-FWP model under investigation are presented in Sect. 2. The results of this study, including the M-FWP energy loss mechanism and M-FWP vortical flow field characteristics, are analyzed in Sect. 3. Finally, concluding remarks and further research recommendations are given in Sect. 4.

2. Numerical methods

2.1 Governing equations and turbulence model

2.1.1 *Governing equations*

In this study, the Reynolds average Navier-Stokes (RANS) equations are employed to simulate the internal flow field of the waterjet pump. The corresponding continuity and momentum conservation equations are expressed as [17,18]

$$\frac{\partial \overline{u}_i}{\partial x_i} = 0, \tag{1}$$

$$\frac{\partial \overline{u}_i}{\partial t} + \overline{u}_j \frac{\partial \overline{u}_i}{\partial x_j} = -\frac{1}{\rho}\frac{\partial p}{\partial x_i} + \nu \frac{\partial^2 \overline{u}_i}{\partial x_j \partial x_j} + \frac{\partial \tau_{ij}}{\partial x_j}, \tag{2}$$

where t is the time, ρ is the fluid density, p is the pressure, ν is the kinematic viscosity, x_i and $\overline{u}_i$ (i = 1, 2, 3) stand for the Cartesian coordinates and corresponding time-averaged velocity components, respectively, and τ_{ij} represents the Reynolds stresses.

2.1.2 *SST k-ω turbulence model*

The SST k-ω turbulence model [19,20] has been adopted to close the momentum equation in the present study. The associated equation for k, namely the turbulent kinetic energy (TKE), is defined as

$$\frac{\partial(\rho k)}{\partial t} + \frac{\partial}{\partial x_i}(\rho \overline{u}_i k) = P_k - \zeta^* \rho k \omega + \frac{\partial}{\partial x_i}\left[(\mu + \sigma_k \mu_t)\frac{\partial k}{\partial x_i}\right]. \tag{3}$$

The ω equation is expressed as

$$\frac{\partial(\rho \omega)}{\partial t} + \frac{\partial}{\partial x_i}(\rho \overline{u}_i \omega) = \chi \rho S^2 - \zeta \rho \omega^2 + \frac{\partial}{\partial x_i}\left[(\mu + \sigma_\omega \mu_t)\frac{\partial \omega}{\partial x_i}\right] + 2\rho(1 - F_1)\frac{\sigma_{\omega 2}}{\omega}\frac{\partial k}{\partial x_i}\frac{\partial \omega}{\partial x_i}, \tag{4}$$

where $\chi = \chi_1 F_1 + \chi_2(1 - F_1)$, and F_1 is determined as

$$F_1 = \tanh\left\{\left[\min\left(\max\left(\frac{\sqrt{k}}{\zeta^* \omega y}, \frac{500\nu}{y^2 \omega}\right), \frac{4\rho\sigma_{\omega 2} k}{CD_{k\omega} y^2}\right)\right]^4\right\}, \tag{5}$$

where $CD_{k\omega}$ is defined as

$$CD_{k\omega} = \max\left(2\rho\sigma_{\omega 2}\frac{1}{\omega}\frac{\partial k}{\partial x_i}\frac{\partial \omega}{\partial x_i}, 10^{-10}\right). \tag{6}$$

In Eq. (3), the turbulence production rate P_k is modeled as

$$P_k = \min\left[\mu_t\frac{\partial \overline{u}_i}{\partial x_j}\left(\frac{\partial \overline{u}_i}{\partial x_j}+\frac{\partial \overline{u}_j}{\partial x_i}\right), 10\zeta^*\rho k\omega\right]. \tag{7}$$

The SST k-ω turbulence model gives the following approximation of the eddy viscosity v_t:

$$v_t = \frac{a_1 k}{\max(a_1\omega, SF_2)}, \tag{8}$$

$$F_2 = \tanh\left\{\left[\max\left(\frac{2\sqrt{k}}{\zeta^*\omega y}, \frac{500v}{y^2\omega}\right)\right]^2\right\}, \tag{9}$$

where $\mu = \rho v$ is the dynamic viscosity, S denotes the invariant measure of the strain rate, and y is the distance to the nearest wall. The constants in this model are given as $a_1 = 0.31$, $\chi_1 = 5/9$, $\chi_2 = 0.44$, $\zeta^* = 0.09$, $\zeta = 0.075$, $\sigma_k = 0.85$, $\sigma_\omega = 0.5$, and $\sigma_{\omega 2} = 0.856$.

2.2 Waterjet pump model

The research object of this study is the AxWJ-2 waterjet pump model. As shown in Fig. 1, the model consists of an inlet pipe, an impeller section, a guide vane section, and an outlet pipe. In order to adapt the flow pattern to the real situation, the inlet and outlet pipes of the original model are extended by 1000 mm. The key parameters of the model are listed in Table 1.

2.3 Meshing

ICEM-CFD and Turbo-Grid were used to generate a structured hexahedral mesh for the entire computational domain. The impeller and guide vane regions were meshed with J and H topologies, respectively. To control the boundary layer distribution near the wall of the pump section, the O-shaped topology was used within the guide vane region and the near-wall region of the pump impeller section [21]. The grid refinement was adopted in these regions to capture the flow details in the near-wall and adjacent zones. This led to the global y^+ value of the first grid over the wall to be smaller than 50. The locally refined grids around the impeller blades and guide vanes are shown in Fig. 2.

Table 1 Geometric and operation parameters of the M-FWP model

Parameters	Values
Inlet pipe outer diameter D_1 (mm)	304.8
Inlet diameter d (mm)	91.44
Outlet pipe outer diameter D_2 (mm)	213.36
Number of impeller blades	6
Number of guide vane blades	8
Design flow Q (L/s)	802
Rotation speed n (r/min)	2000

2.4 Boundary conditions

In the present study, simulations were performed using the commercial software ANSYS-Fluent. The finite volume method (FVM) was applied for spatial discretization of the governing equations. The SIMPLEC algorithm was utilized as the pressure-velocity coupling method. The inlet boundary condition was specified as "the mass flow in", while the outlet boundary condition was specified as "the static pressure out". The impeller component was characterized as the integrally rotating domain and the hub was specified to be fixed. A no slip wall was specified for the wall boundary, and the areas near the walls were treated by standard wall functions. The calculation was deemed to converge when the absolute residual falls below 10^{-5}.

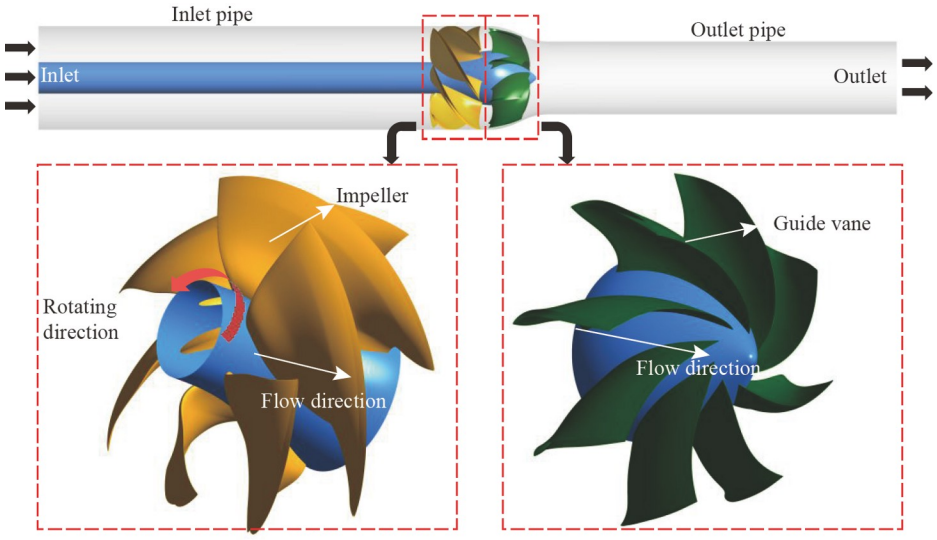

Figure 1 Three-dimensional model of the M-FWP.

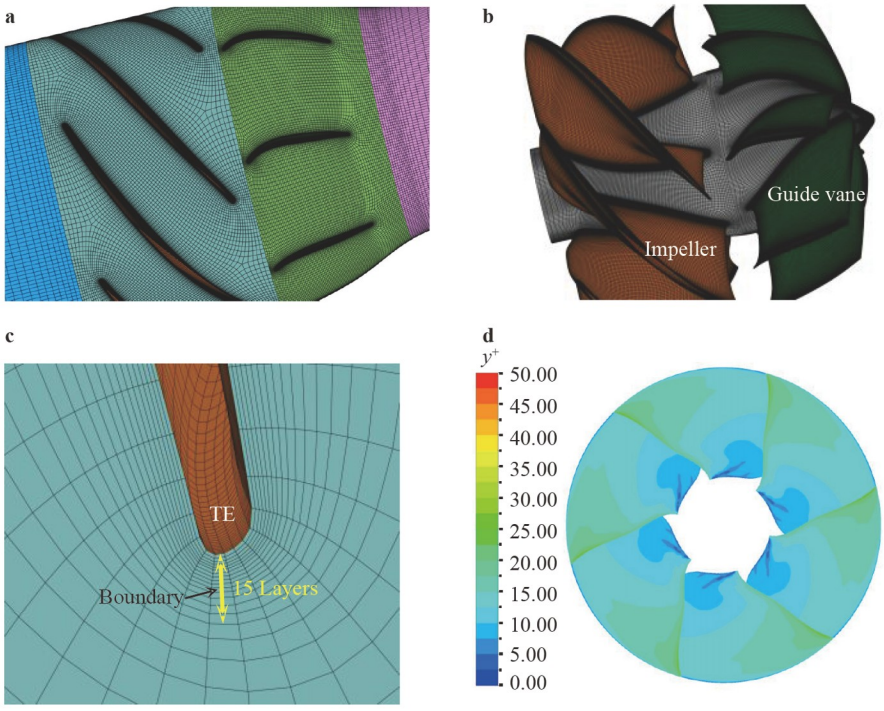

Figure 2 Information of grids for performing the numerical simulation. **a** External local grids. **b** Internal local grids. **c** Schematic representation of the grid near the wall. **d** Contours of the y^+ value of the first grid near the impeller blade.

2.5 Grid independence verification

Grid independence was verified based on the Richardson extrapolation method, and grid convergence index (GCI) was used to analyze the error quantitatively [22-24]. Three sets of grids with 4.05 million, 8.91 million, and 19.62 million cells were considered. The pump delivery head H and efficiency η were selected for the grid error analysis. The corresponding characteristic parameters are defined as

$$H = \frac{p_2 - p_1}{\rho g}, \tag{10}$$

$$\eta = \frac{\rho g Q H}{P_t}, \quad P_t = \frac{nM}{9.55}, \tag{11}$$

where p_1 and p_2 denote the pressure at the inlet and outlet of the pump unit, respectively, η is the pump efficiency, Q is the flow rate, P_t is the total input power, n is the revolving speed, and M is the torque of the impeller blades.

Table 2 lists the GCI calculation results. As shown, using head and efficiency as evaluation parameters, the fine-grid convergence indices are 0.105% and 0.651%, respectively. Considering the calculation accuracy and cost [25], the total number of grids was finally chosen to be 8.91 million.

Table 2 Verification of grid independence

Parameters	$\varphi = H$	$\varphi = \eta$
N_1	19625483	
N_2	8910748	
N_3	4055739	
Mesh refinement factor, r_{21}	1.3	
Mesh refinement factor, r_{32}	1.3	
Numerical solution, φ_1	22.555 m	90.655%
Numerical solution, φ_2	22.536 m	90.601%
Numerical solution, φ_3	22.498 m	90.516%
Extrapolated value, φ_{ext}	22.574 m	90.713%
Extrapolation error, e_{ext}	0.08%	0.06%
Grid convergence index, GCI_{fine}	0.105%	0.651%

3. Results analyses

3.1 Validation against experimental results

In the present numerical simulation, eight flow rates ranging from 500 kg/s to 1000 kg/s are selected to calculate the corresponding head and efficiency. Figure 3 depicts the comparison between simulation and experimental results in terms of the pump delivery head H and efficiency η, under different flow-rate operation conditions. As shown, the variations of both H and η with respect to the flow rate Q predicted by the simulation are in general consistent with experimental results, particularly near the best efficiency operating point (Q_{BEP}). The relative difference is smaller than 3% at all flow rates.

3.2 Energy loss

3.2.1 Entropy production theory

Hydraulic losses are usually accompanied by an increase in

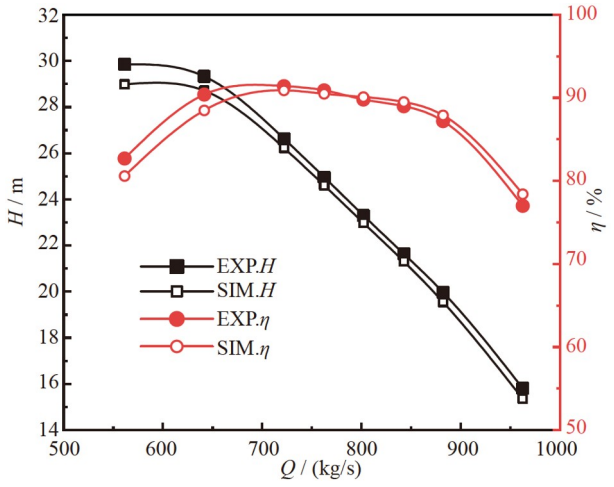

Figure 3 Comparison of pump delivery head H and efficiency η between the experimental and simulation results. The left and right scales indicate the values of H and η, respectively.

entropy. According to the second law of thermodynamics, the resulting hydraulic losses are irreversible, and the entire system generates irreversible energy dissipation. Therefore, the relationship between energy dissipation and entropy production can be established, and the energy loss in the flow process can be well predicted by the entropy production theory.

The entropy production equation in Cartesian coordinates can be written as [26-28]

$$\frac{\dot{Q}}{T} = \dot{S}_D''' = \dot{S}_{\overline{D}}''' + \dot{S}_{D'}''', \tag{12}$$

where $\dot{Q}$ is the energy transfer rate, T is the temperature, $\dot{S}_D'''$ is the total entropy production rate (TEP), which can be decomposed into $\dot{S}_{\overline{D}}'''$ and $\dot{S}_{D'}'''$, namely, the contributions from the direct dissipation (EPDD) and turbulence dissipation (EPTD), respectively, defined as

$$\dot{S}_{\overline{D}}''' = \frac{2\mu}{T}\left[\left(\frac{\partial \overline{u}_1}{\partial x_1}\right)^2 + \left(\frac{\partial \overline{u}_2}{\partial x_2}\right)^2 + \left(\frac{\partial \overline{u}_3}{\partial x_3}\right)^2\right] + \frac{\mu}{T}\left[\left(\frac{\partial \overline{u}_2}{\partial x_1} + \frac{\partial \overline{u}_1}{\partial x_2}\right)^2 + \left(\frac{\partial \overline{u}_3}{\partial x_1} + \frac{\partial \overline{u}_1}{\partial x_3}\right)^2 + \left(\frac{\partial \overline{u}_2}{\partial x_3} + \frac{\partial \overline{u}_3}{\partial x_2}\right)^2\right], \tag{13}$$

$$\dot{S}_{D'}''' = \frac{2\mu_{\text{eff}}}{T}\left[\left(\frac{\partial u_1'}{\partial x_1}\right)^2 + \left(\frac{\partial u_2'}{\partial x_2}\right)^2 + \left(\frac{\partial u_3'}{\partial x_3}\right)^2\right] + \frac{\mu_{\text{eff}}}{T}\left[\left(\frac{\partial u_2'}{\partial x_1} + \frac{\partial u_1'}{\partial x_2}\right)^2 + \left(\frac{\partial u_3'}{\partial x_1} + \frac{\partial u_1'}{\partial x_3}\right)^2 + \left(\frac{\partial u_2'}{\partial x_3} + \frac{\partial u_3'}{\partial x_2}\right)^2\right]. \tag{14}$$

In Eq. (14), u_i' (i = 1, 2, 3) represents the velocity fluctuations, and μ_{eff} stands for the effective dynamic viscosity of fluid, which is calculated as

$$\mu_{\text{eff}} = \mu + \mu_t, \tag{15}$$

where $\mu_t = \rho \nu_t$ is the turbulence dynamic viscosity. Combined with the k-ω turbulence model given by Eqs. (3) and (4), the EPTD can be further expressed as a function of density ρ, TKE k, and turbulent vortex frequency ω *as* [14,29,30]

$$\dot{S}_{D'}''' = \gamma \frac{\rho \omega k}{T}, \tag{16}$$

where γ = 0.99 is the constant of the SST model.

The bulk entropy production rates in the main flow region caused by the mean and fluctuating velocities can be obtained by integrating the EPDD and EPTD over the entire computational domain as

$$\dot{S}_{\overline{D}} = \int_V \dot{S}_{\overline{D}}''' \mathrm{d}V, \tag{17}$$

$$\dot{S}_{D'} = \int_V \dot{S}_{D'}''' \mathrm{d}V. \tag{18}$$

In addition to these two parts, there is a peak value of the entropy production rate in the near-wall region with $y^+ < 50$, which is not accurately captured in conventional RANS methods. Duan et al. [31,32] proposed a wall function for evaluating the near-wall entropy production rate as

$$\dot{S}_W = \int_A \frac{\tau_w \cdot u_w}{T} \mathrm{d}A, \tag{19}$$

where $\dot{S}_W$ denotes the entropy production rate caused by wall shear stress (EPWS), τ_w represents the wall shear stress, and u_w is the velocity at the first grid over the wall.

The TEP is then expressed as

$$S_{\text{Total}} = \dot{S}_{\overline{D}} + \dot{S}_{D'} + \dot{S}_W. \tag{20}$$

In Eqs. (17)-(19), V and A represent the control volume and control surface, respectively, for performing the integrations. Assuming that the temperature remains constant, the irreversible energy loss rate Q_{iel} in the pump can be evaluated as

$$Q_{\text{iel}} = TS_{\text{Total}}. \tag{21}$$

The energy loss rate can be also expressed in the form of hydraulic loss as

$$H_{\text{hl}} = \frac{TS_{\text{Total}}}{q_{\text{m}} g}, \tag{22}$$

where q_{m} denotes the mass flow rate, and g is the gravitational acceleration.

3.2.2 *Comparative analysis based on entropy production and differential pressure methods*

The entropy production in the entire domain is the integration of TEP (Eq. (20)) that quantifies the total energy loss. To assess the accuracy of the energy loss given by the entropy production theory, the hydraulic losses calculated according to the entropy production method (H_{ep}) are compared with those calculated according to the differential pressure method (H_{dp}). Likewise, the pump efficiency calculated using the entropy production method (η_{ep}) is com-

pared with that calculated using the differential pressure method (η_{dp}). Both comparisons are shown in Fig. 4. It can be seen that both the hydraulic losses and the pump efficiency calculated using two different methods are in good agreement. Figure 4a shows that as the flow rate increases, the hydraulic loss first decreases and then increases to its maximum value at the largest flow rate considered in the present study. On the other hand, the efficiency (Fig. 4b) first increases, reaching its peak value near Q_{BEP} with small hydraulic loss, and then decreases as the flow rate continues to decrease. The relative differences in both H and η between two different calculation approaches are smaller than 5% under all flow-rate operation conditions. This indicates that the entropy production method is reliable to predict the performance of the M-FWP.

3.2.3 *The varying law of entropy production*

Figure 5 compares the magnitude of the entropy production loss under various flow-rate operation conditions. It is seen that the hydraulic loss caused by turbulence dissipation (h_{TD}) makes the largest proportion of contribution, and its variation with respect to the flow rate dominates the total hydraulic loss. Specifically, the hydraulic loss caused by turbulence dissipation also decreases first and then increases as the flow rate increases. Of secondary importance is the hydraulic loss corresponding to the wall dissipation (h_{WS}), which increases monotonically with the flow rate, since the increase of flow rate tends to induce larger velocity gradients at the wall. The hydraulic loss induced by the direct dissipation (h_{DD}) is relatively small in comparison with the other two components, and remains almost unchanged at different flow rates.

According to the above observation that the turbulence dissipation dominates the hydraulic loss, we further compare its distribution in different sections of the M-FWP in Fig. 5b. It is seen that the variation trends of turbulence

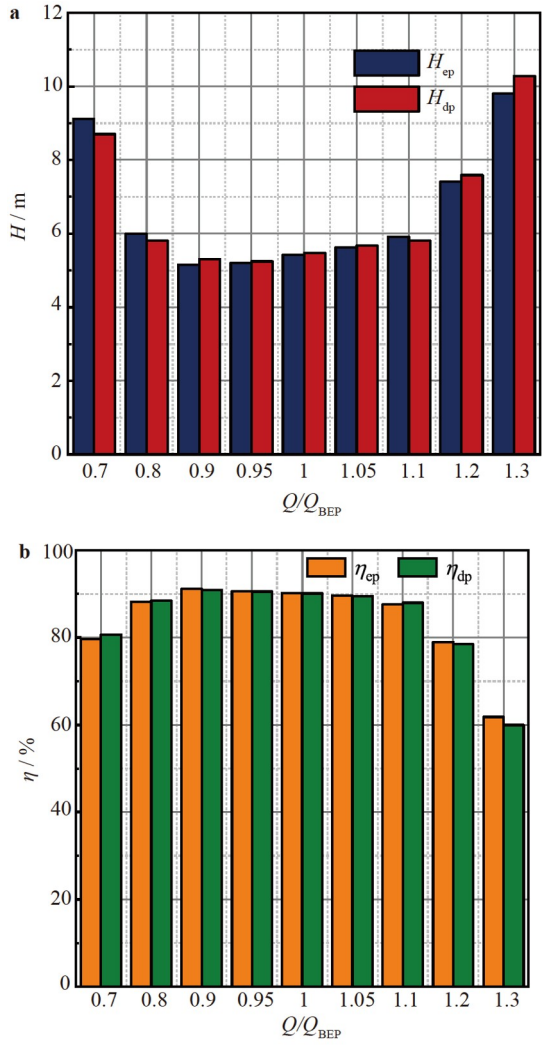

Figure 4 Comparison of hydraulic loss and pump efficiency between entropy production method and differential pressure method. **a** Hydraulic loss. **b** Pump efficiency.

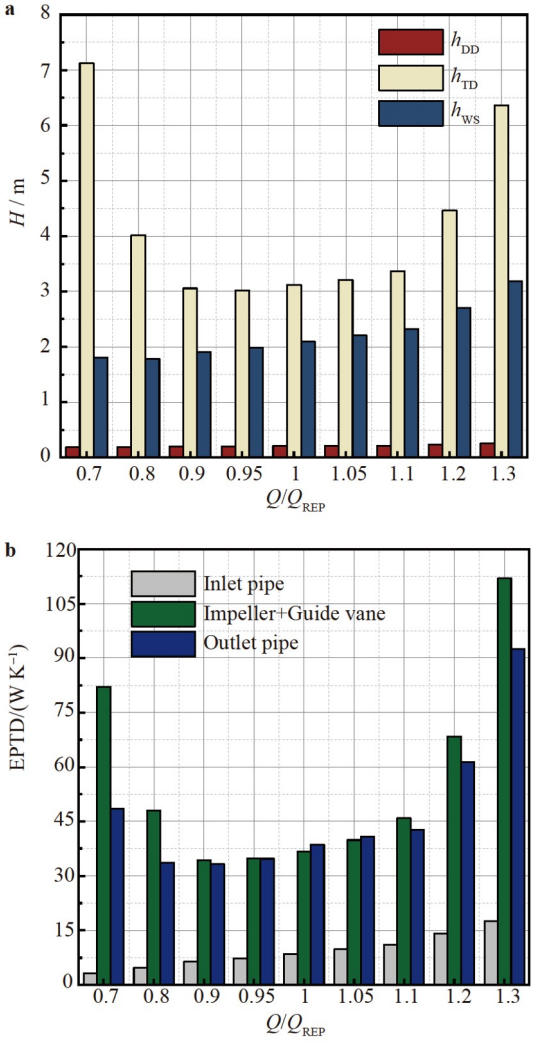

Figure 5 Distribution law of entropy production and loss. **a** Hydraulic loss of each entropy production term. **b** Turbulence dissipation of each component.

dissipation in the impeller/guide vane section and in the outlet pipe section remain the same as the total hydraulic loss. They all decrease first and then increase as the flow rate increases. However, when the flow rate deviates from the optimal condition, the turbulence dissipation in the impeller/guide vane section becomes significantly larger than that in the outlet pipe. In this sense, the turbulence dissipation in the impeller/guide vane section is primarily responsible for the increase of energy losses when the M-FWP is operated at non-optimal conditions. Compared to the impeller/guide vane section and the outlet pipe, the turbulence dissipation in the inlet pipe is relatively small. This is because the turbulence dissipation correlates with the fluctuating velocity in the impeller/guide vane and outlet sections, while the turbulence intensity in the inlet pipe is relatively weak.

3.2.4 *Generation mechanism of turbulence dissipation*

To investigate the mechanism underlying the energy loss induced by turbulence dissipation, Fig. 6-8 further show the streamlines, contours of vorticity, TKE, and turbulence dissipation under various flow-rate operation conditions. Panels a-c in these figures show the results at different spans. Specifically, panel a shows the results at span = 0.1, which is near the blade root of the impeller and guide vanes. Panel b shows span = 0.5 in the core region between the hub and the pipe casing. Panel c shows span = 0.9 near the tip of the impeller and guide vanes. In this study, 0.1, 0.5 and 0.9 spans are selected as the typical areas, which can show the flow characteristics near the tip, middle and root of the blade, respectively. In the impeller section, considering the impeller rotation, U, V, and W are used to denote the cir-

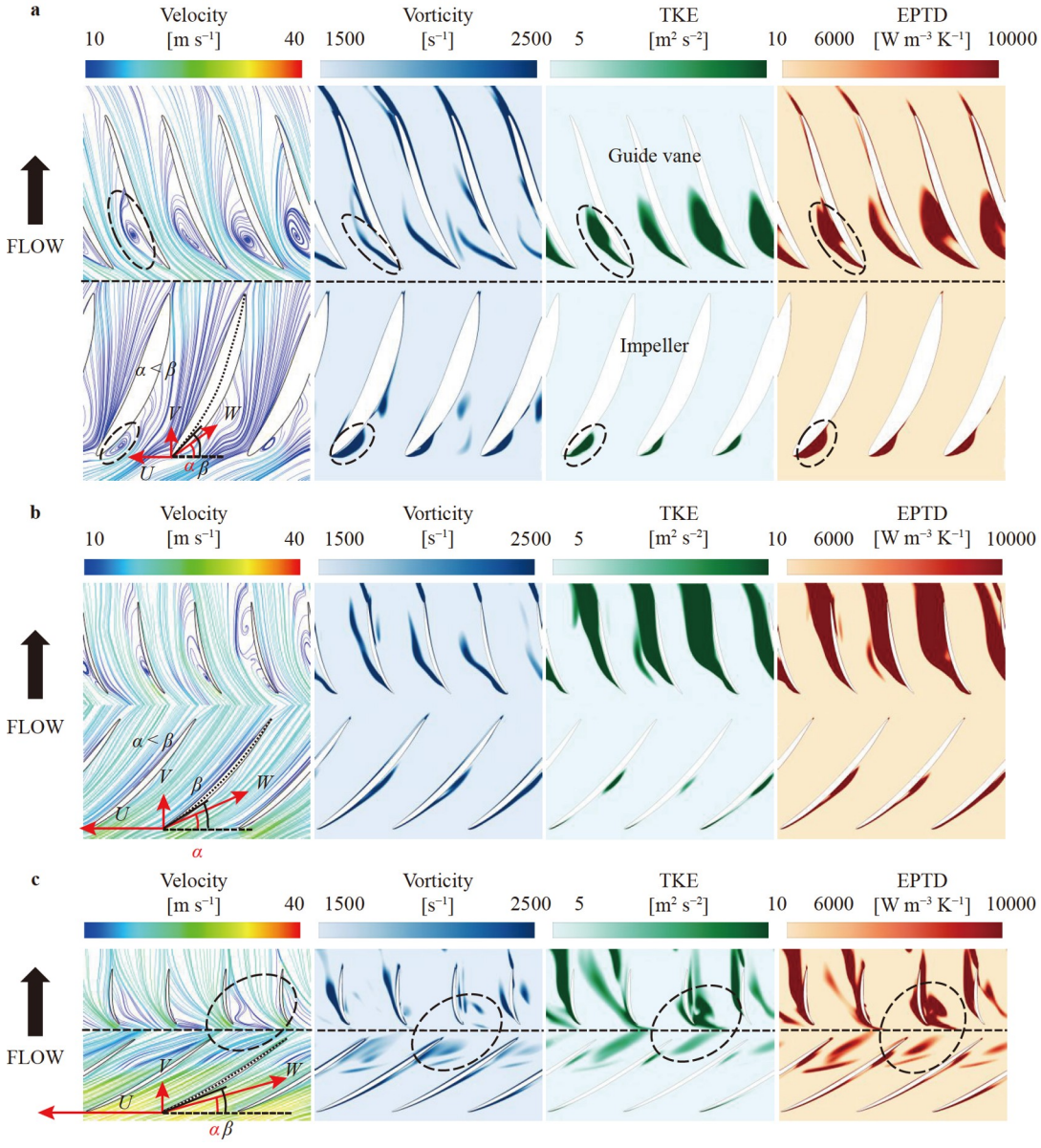

Figure 6 Streamlines, vorticity, TKE, and EPTD at different span sections under $Q = 0.7\ Q_{BEP}$. **a** span = 0.1. **b** span = 0.5. **c** span = 0.9.

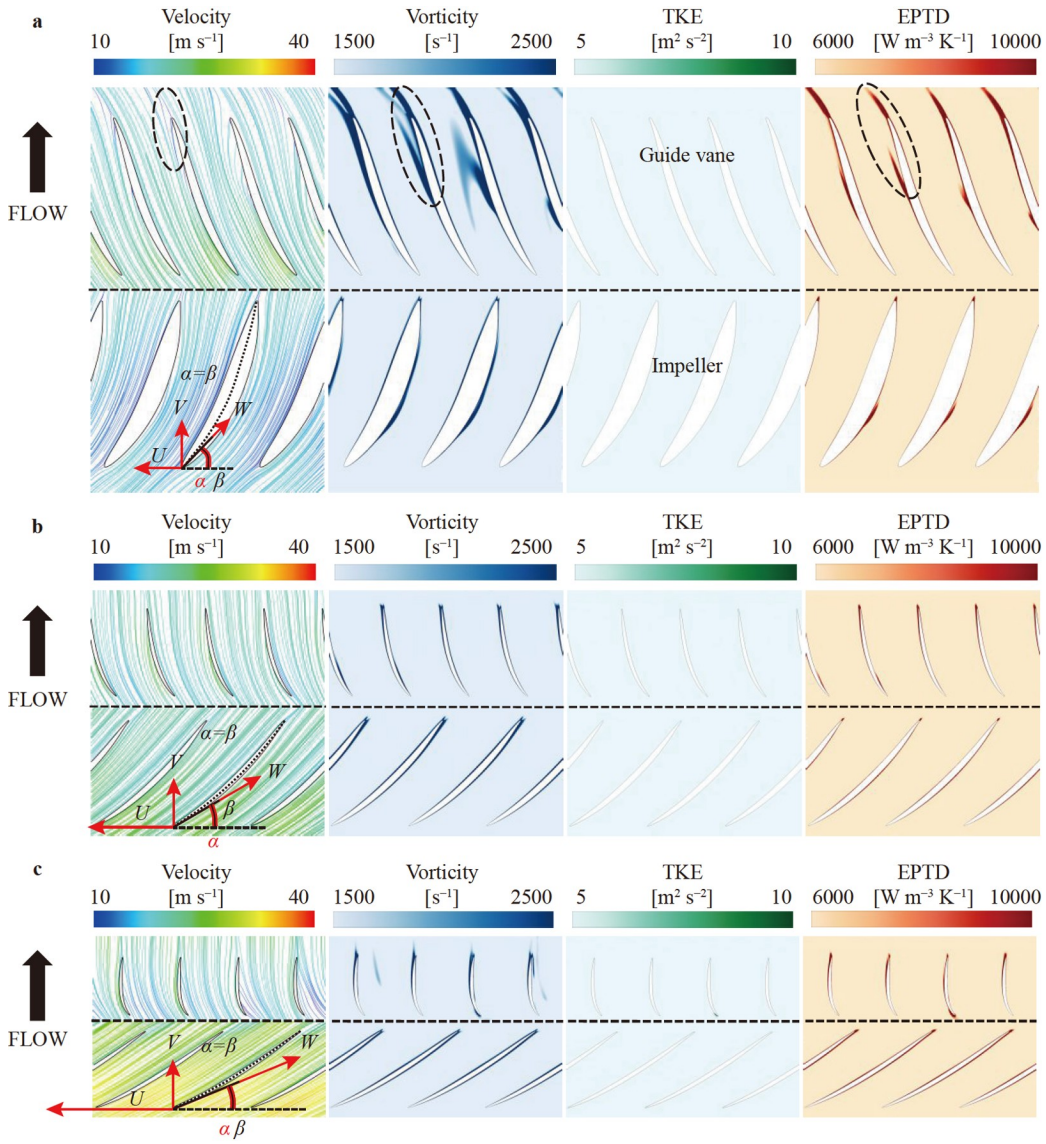

Figure 7 Streamlines, vorticity, TKE, and EPTD at different span sections under $Q = 1.0Q_{BEP}$. **a** span = 0.1. **b** span = 0.5. **c** span = 0.9.

cumferential velocity, absolute velocity, and relative velocity of the water flow, respectively; while α and β are the water inflow angle and the blade inlet angle, respectively.

Under the low flow-rate operation condition $Q = 0.7Q_{BEP}$, as shown in Fig. 6, in the impeller section, due to the small entrance velocity, the angle of the water flow α is smaller than the blade inlet angle β, which causes flow separation on the suction side, forming a vortex sheet, and correspondingly, strong TKE and dissipation. And the streamlines are distorted in the guide vane section, particularly on the suction side, indicating the occurrence of flow separation there, which is also evident from the detached vortices at the leading edge of the blade. The separation bubble covers almost the entire blade, resulting in large TKE and dissipation on the suction side. In the span near the blade tip (Fig. 6c), some distorted streamlines extend to the pressure side of the neighboring blade, leading to an enhancement of TKE and dissipation there.

As the flow rate increases to the optimal operation condition, the water incidence angle at blade leading edge is almost identical to the blade inlet angle. The streamlines closely follow the geometry of the blade surfaces in both impeller and guide vane sections, except for a slight distortion from center to the trailing edge of the blade root in the guide vane section at span = 0.1 (Fig. 7a). Accordingly, TKE and dissipation are only active in a thin boundary layer near the blade, while their magnitudes are relatively small in the main body of the flow passage. As a result, the bulk dissipation is low under the optimal flow-rate condition.

When the pump flow rate further increases to a larger value, Fig. 8 shows that the water incidence angle is greater than the blade inlet angle in the impeller section, such that low-speed flow zone form on the BPS near the blade tip, causing flow separation and strong turbulence dissipation.

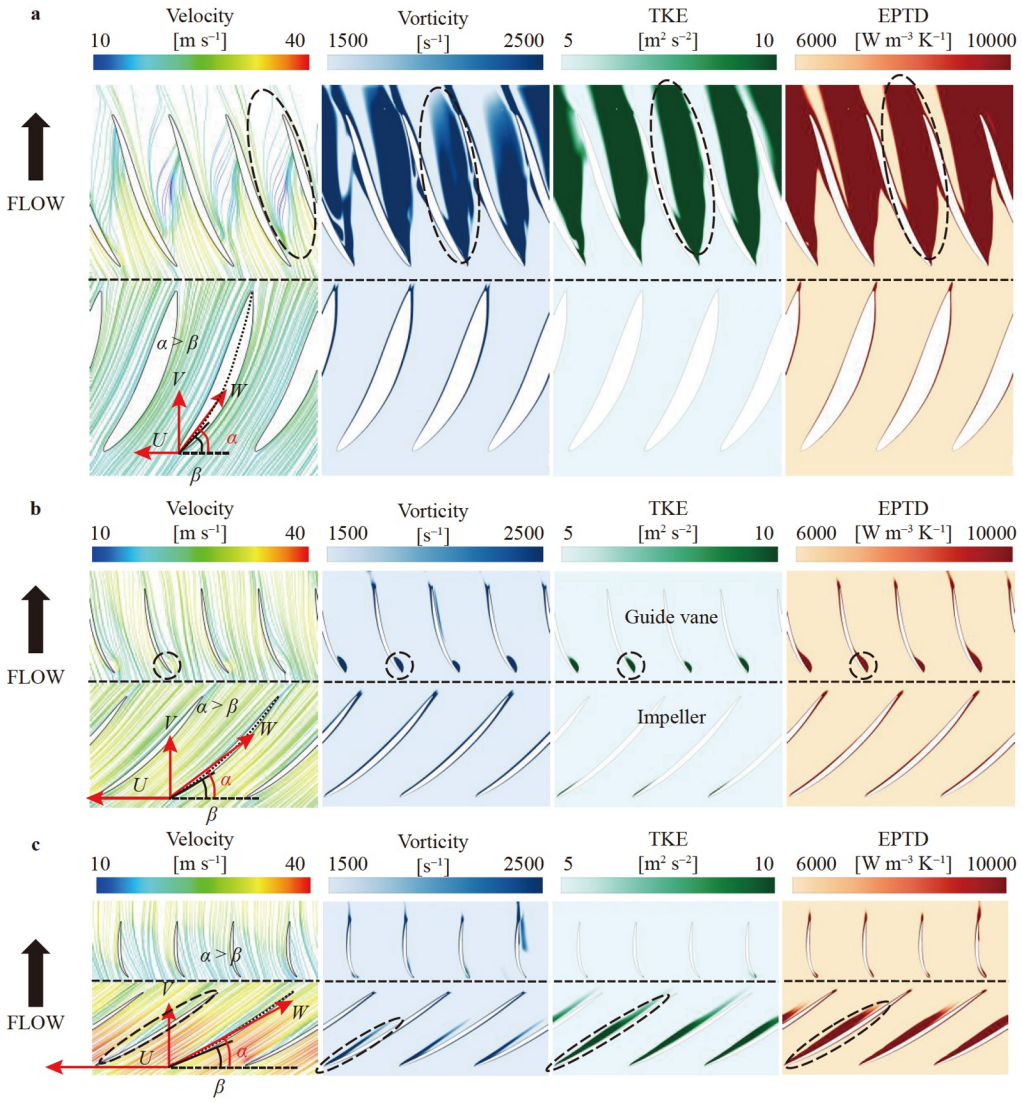

Figure 8 Streamlines, vorticity, TKE, and EPTD at different span sections under $Q = 1.3Q_{\mathrm{BEP}}$. **a** span = 0.1. **b** span = 0.5. **c** span = 0.9.

And the streamlines in the guide vane section near the blade root become rather distorted, causing flow separation there, and high TKE and dissipation region almost occupies the entire flow passage between the blades.

In summary of the above analyses on different physical quantities in the impeller and guide vane sections, it is evident that the flow regions with large vortices and flow separations are highly consistent with strong TKE and dissipation. It can be therefore inferred that hydraulic phenomena such as eddy currents and flow separations are responsible for the enhancement of turbulence dissipation. In addition, the flows in different passages are different, due to the flow with high Reynolds number is actually unsteady. And the phenomena can be found in many studies using RANS to simulate and analyze the characteristics of the main flow in rotating machinery [26,28,33]. Nonetheless, the local unsteady flow does not affect the evaluation of the time-averaged energy loss caused by the main flow. Due to the flow separation, large velocity gradient zones occur in the flow passage, leading to subsequent generation of shear stresses on the fluid particles, causing them to rotate and generating large vortices in the corresponding areas. These unsteady flows cause the TKE to increase, resulting in greater turbulence dissipation. When the pump is operated under the optimal operation condition, the flow separation is less significant, such that the turbulence dissipation in the flow passage is minimized, and so is the hydraulic loss.

3.3 Transport equation of enstrophy

To further analyze the causes of turbulent dissipation and its relationship with vortices, the transport equation of enstrophy of time-averaged vorticity is examined in the guide vane and impeller sections. Here, the enstrophy is defined as $\overline{\Omega} = \overline{\omega}_i\overline{\omega}_i / 2$, with $\overline{\omega}_i$ (i = 1, 2, 3) being the time-averaged vorticity. The transport equation of $\overline{\Omega}$ is expressed as

$$\frac{\partial(\overline{\omega}_i\overline{\omega}_i/2)}{\partial t} = G_\omega + R_\omega + C_\omega + B_\omega + V_\omega. \tag{23}$$

The first term on the right hand side of Eq. (23) is the relative vortex generation term, expressed as

$$G_\omega = \overline{\omega}_i\overline{S}_{ij}\overline{\omega}_j - \overline{u}_j\frac{\partial(\overline{\omega}_i\overline{\omega}_i/2)}{\partial x_j}. \tag{24}$$

This term represents the generation of vorticity induced by velocity gradients, with $\overline{S}_{ij} = \left(\partial\overline{u}_j/\partial x_i + \partial\overline{u}_i/\partial x_j\right)/2$ being the time averaged strain-rate tensor. The second term is the Reynolds stress dissipation term. According to the Boussinesq hypothesis, it can be estimated as

$$R_\omega = \nu_t\left(\frac{\partial^2\overline{\omega}_i}{\partial x_j\partial x_j}\overline{\omega}_i + \frac{\partial^2\overline{\omega}_j}{\partial x_j\partial x_i}\overline{\omega}_i\right) - \frac{2}{3}\varepsilon_{ijk}\frac{\partial^2 k}{\partial x_i\partial x_j}\overline{\omega}_k, \tag{25}$$

which influences enstrophy in terms of turbulent dissipation, with ε_{ijk} being the alternating tensor. The third term is the Coriolis force term, defined as

$$C_\omega = -2\left(\frac{\partial(c_i\overline{u}_j)}{\partial x_j}\overline{\omega}_i - \frac{\partial(c_i\overline{u}_j)}{\partial x_i}\overline{\omega}_j\right), \tag{26}$$

which is related to the rotational motion of the impeller, with c being the angular velocity. This term is trivial in the guide vane section. The fourth term is the baroclinic torque:

$$B_\omega = \frac{1}{\rho^2}\varepsilon_{ijk}\overline{\omega}_i\frac{\partial\rho}{\partial x_j}\frac{\partial p}{\partial x_k}, \tag{27}$$

which accounts for the change in vortex volume due to the nonparallelism of the pressure and density gradients. This term is trivial in the present study because of the constant density value. The last term is the viscous term, expressed as

$$V_\omega = \nu\frac{\partial^2\overline{\omega}_i}{\partial x_j\partial x_j}\overline{\omega}_i, \tag{28}$$

which represents the change in the vorticity due to the fluid viscous effects.

To investigate the mechanism of vorticity dynamics, Fig. 9 shows the contours of the non-zero terms in Eq. (23) at optimal flow-rate operation conditions. In Fig. 9, the relative

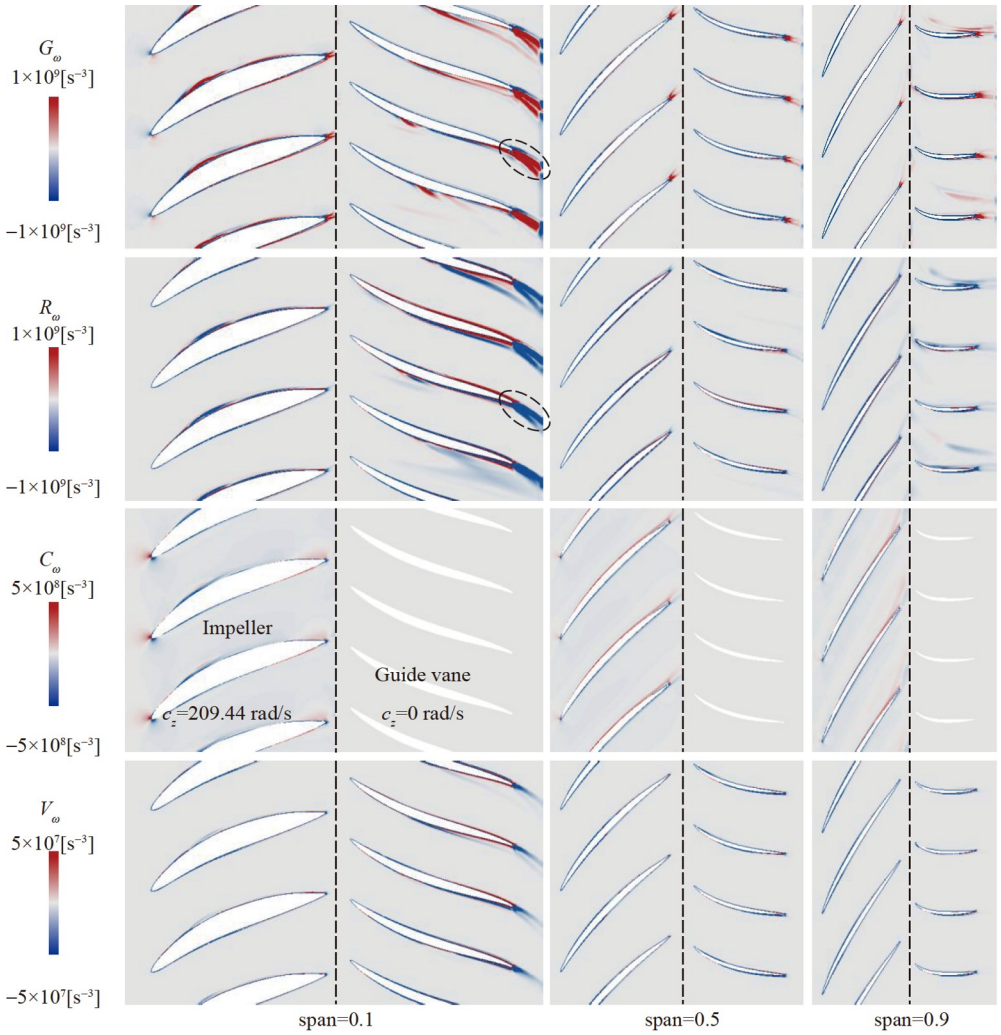

Figure 9 Distribution of the relative vortex generation term, the Reynolds stress diffusion term, the Coriolis force term and the viscous term at different span sections under $Q = 1.0Q_{BEP}$.

vortex generation term G_ω and the Reynolds stress dissipation term R_ω are the primary causes of the vorticity generation and dissipation. The regions with their large amplitudes are mainly distributed at the trailing edge of the blades, particularly near the hub with span = 0.1. The Coriolis force terms C_ω are distributed in the impeller flow domain. In the guide vane section, the value of C_ω is zero because C_ω is related to the system rotation, but the guide vanes are static. The magnitude of the viscous term V_ω is smaller than that of G_ω and R_ω.

Since the relative vortex generation term is the primary cause of the vorticity growth, Fig. 10 further compares the contours of the vortex generation term at different flow-rate operation conditions. From Fig. 10a, it is seen that under the low flow-rate operation condition $Q = 0.7Q_{BEP}$, the magnitude of the relative vortex generation term G_ω is larger in both the impeller and guide vane sections than under the optimal flow-rate operation condition $Q = 1.0Q_{BEP}$ at all spans. In the impeller section, large G_ω almost covers the blade leading edge and the adjacent portion of its suction surface. In the guide vane section, the large magnitude of G_ω is concentrated at the leading edge of the blade near the suction surface and extends downstream. Figure 10c shows that under the large flow-rate operation condition $Q = 1.3Q_{BEP}$, the large magnitude of G_ω is confined to the near-hub region with span = 0.1 of the guide vane section. There are two dominant regions with large magnitude of G_ω in the guide vane section. As shown in the lower left figure, the first region originates from the leading edge of the guide vane, extends obliquely downstream, and attaches to the suction side of the adjacent blade. The second region occurs around the trailing edge of the blade, almost filling the entire flow passage between two blades.

4. Conclusion

In the present study, numerical simulations of the steady

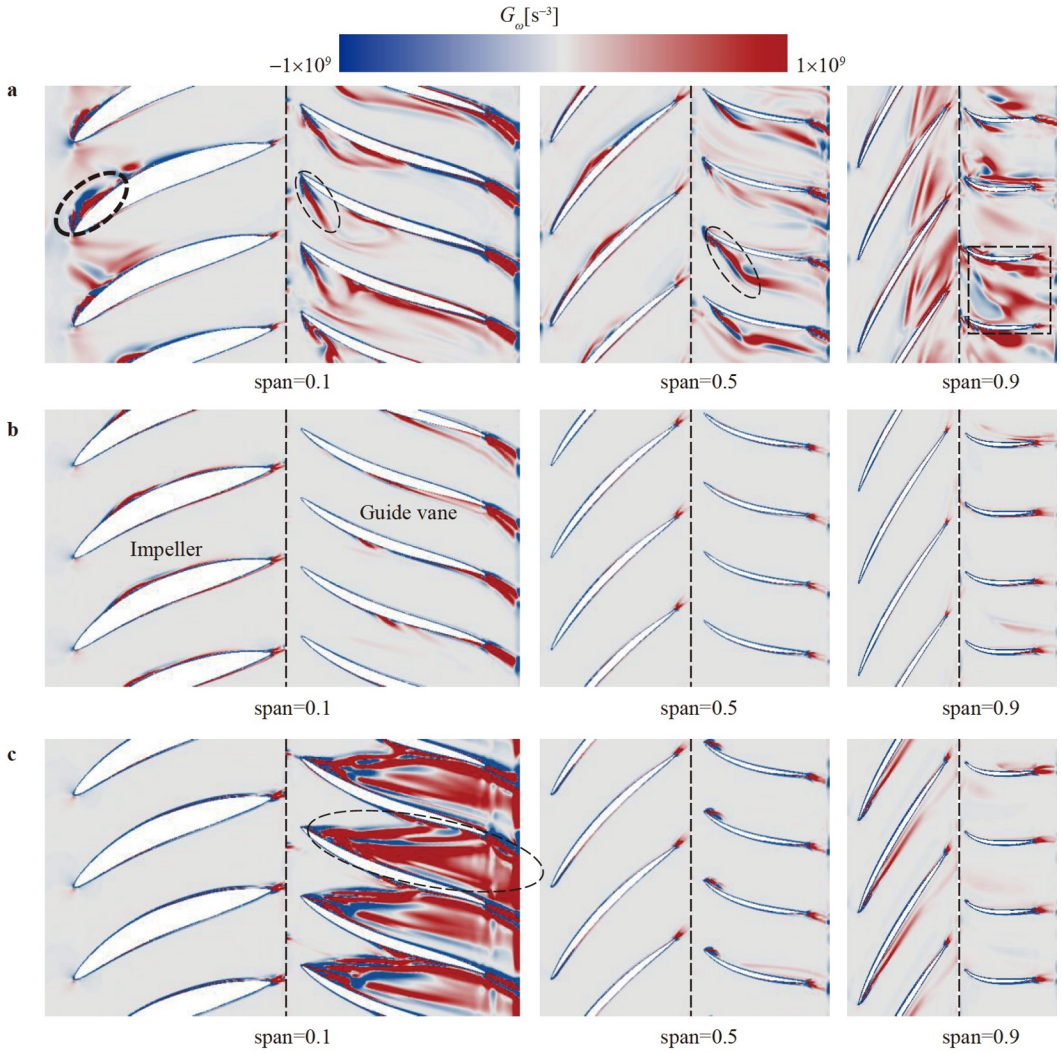

Figure 10 Distribution of the relative vortex generation term at low $Q = 0.7Q_{BEP}$, optimal $Q = 1.0Q_{BEP}$, and large $Q = 1.3Q_{BEP}$ flow-rate operation conditions. **a** $Q = 0.7Q_{BEP}$. **b** $Q = 1.0Q_{BEP}$. **c** $Q = 1.3Q_{BEP}$.

flow across an M-FWP under different flow-rate operation conditions are performed. Using the entropy production theory, the energy loss mechanism within the pump flow passages is investigated. Analyses of the transport equation of the enstrophy provide a deeper understanding of the process of vorticity generation. The main findings of the present study are summarized as follows.

(1) The energy loss estimation based on the entropy production theory provides additional information compared to the traditional differential pressure method, especially about the location of the energy loss. From a performed comparative analysis of different entropy production parts, it emerges that the turbulence dissipation contributes most to the energy loss within the impeller and guide vane sections, followed by wall dissipation, and direct dissipation. The overall turbulence dissipation of the pump is mainly contributed by the impeller and the guide vanes section, followed by the outlet pipe. It is also found that the energy loss depends strongly on the operation condition. The turbulence dissipation is smallest under the optimal conditions, and increases when the flow rate deviates from the optimal operation condition.

(2) By comparing the correlation of velocity gradient, vorticity, turbulence intensity and turbulence dissipation with the entropy production in the flow field, it is found that unstable flow phenomena such as flow separation and large-scale vortices are highly correlated to the turbulence dissipation. Under the low flow-rate operation condition, the water flow hits the inlet pressure surface of the impeller blade, resulting in a significant flow separation on the back of the blade at all spans. Under the large flow-rate operation condition, streamlines are distorted near the blade root of the guide vane section. Significant flow separation and large-scale vortices lead to large magnitude of TKE, leading to strong turbulence dissipation in the corresponding regions.

(3) By analyzing the transport equation of enstrophy of time-averaged vorticity, it is found that the relative vortex generation term plays a leading role in the generation of enstrophy within the pump's flow passages, with its effect mainly balanced by the Reynolds stresses dissipation term. The Coriolis force term and viscous term make relatively small contributions to the balance of the enstrophy. Under the optimal flow-rate operation condition, the relative vortex generation term is only active in the vicinity of the blades of the impeller and guide vane. Under the small flow-rate operation condition, large relative vortex generation term almost covers the blade leading edge and the adjacent portion of its suction surface at all spans. Under the large flow-rate operation condition, the large amplitude of the relative vortex generation term occupies the flow passage between two blades near the hub of the guide vane section.

Author contributions *Kan Kan designed the research, offered methodology and computing resources, carried out all the simulations and results analysis, wrote the first draft of the manuscript, and offered funding acquisition. Yuhang Xu carried out all the simulations and results analysis, wrote the first draft of the manuscript. Hui Xu offered computing resources, verified the results, wrote the first draft of the manuscript and supervised the research. Jianggang Feng offered computing resources, verified the results and supervised the research. Zixuan Yang designed the research, offered methodology, analyzed the results, supervised the research, offered funding acquisition and revised the final version.*

Acknowledgements *This work was supported by the National Natural Science Foundation of China (Grant Nos. 52009033 and 11972038), the Natural Science Foundation of Jiangsu Province (Grant No. BK20200509), and the Postdoctoral Research Foundation of China (Grant Nos. 2022M711021 and 2021M690876).*

1 W. G. Park, J. H. Jang, H. H. Chun, and M. C. Kim, Numerical flow and performance analysis of waterjet propulsion system, Ocean Eng. **32**, 1740 (2005).
2 R. Huang, R. Zhang, Y. Wang, X. Luo, and L. Zhu, Experimental and numerical investigations into flow features in an intake duct for the waterjet propulsion under mooring conditions, Acta Mech. Sin. **37**, 826 (2021).
3 J. Hong, and A. Abraham, Snow-powered research on utility-scale wind turbine flows, Acta Mech. Sin. **36**, 339 (2020).
4 M. Zhang, F. Feng, M. Wang, Z. Guo, Z. Kang, and B. Huang, Investigation of hysteresis effect of cavitating flow over a pitching Clark-Y hydrofoil, Acta Mech. Sin. **38**, 321382 (2022).
5 W. Liu, Z. Ji, D. Guo, G. Yang, G. Zhou, and K. Ren, Effects of bottom deflectors on aerodynamic drag reduction of a high-speed train, Acta Mech. Sin. **38**, 321251 (2022).
6 H. Wu, F. Soranna, T. Michael, J. Katz, and S. Jessup, Cavitation in the tip region of the rotor blades within a waterjet pump, Fluids Eng. Div. Summer Meet. **48418**, 193 (2008).
7 H. Wu, R. L. Miorini, and J. Katz, Analysis of turbulence in the tip region of a waterjet pump rotor, Fluids Eng. Div. Summer Meet. **49484**, 699 (2010).
8 H. Wu, R. L. Miorini, and J. Katz, Measurements of the tip leakage vortex structures and turbulence in the meridional plane of an axial water-jet pump, Exp. Fluids **50**, 989 (2011).
9 R. L. Miorini, H. Wu, and J. Katz, The internal structure of the tip leakage vortex within the rotor of an axial waterjet pump, In Turbo Expo: Power for Land, Sea, and Air **44021**, 403 (2010).
10 Q. Guo, X. Huang, and B. Qiu, Numerical investigation of the blade tip leakage vortex cavitation in a waterjet pump, Ocean Eng. **187**, 106170 (2019).
11 R. Huang, B. Ji, X. Luo, Z. Zhai, and J. Zhou, Numerical investigation of cavitation-vortex interaction in a mixed-flow waterjet pump, J. Mech. Sci. Technol. **29**, 3707 (2015).
12 R. Huang, Y. Wang, T. Du, X. Luo, W. Zhang, and Y. Dai, Mechanism analyses of the unsteady vortical cavitation behaviors for a waterjet pump in a non-uniform inflow, Ocean Eng. **233**, 108798 (2021).
13 P. Cao, Y. Wang, C. Kang, G. Li, and X. Zhang, Investigation of the role of non-uniform suction flow in the performance of water-jet pump, Ocean Eng. **140**, 258 (2017).
14 H. Herwig, D. Gloss, and T. Wenterodt, A new approach to understanding and modelling the influence of wall roughness on friction factors for pipe and channel flows, J. Fluid Mech. **613**, 35 (2008).
15 H. Guan, W. Jiang, Y. Wang, H. Tian, T. Li, and D. Chen, Numerical simulation and experimental investigation on the influence of the clocking effect on the hydraulic performance of the centrifugal pump as turbine, Renew. Energy **168**, 21 (2021).
16 B. Yang, B. Li, H. Chen, and Z. Liu, Entropy production analysis for the clocking effect between inducer and impeller in a high-speed centrifugal pump, Proc. Inst. Mech. Eng. Part C-J. Mech. Eng. Sci. **233**, 5302 (2019).

17 K. Kan, H. Chen, Y. Zheng, D. Zhou, M. Binama, and J. Dai, Transient characteristics during power-off process in a shaft extension tubular pump by using a suitable numerical model, Renew. Energy **164**, 109 (2021).
18 S. Shen, Z. Qian, and R. K. Agarwal, in Numerical analysis of fluid dynamics of tip leakage vortex with different gap widths in an axial flow pump: Proceedings of the 2018 AIAA Aerospace Sciences Meeting, Kissimmee, 2018.
19 Y. Wang, and W. J. Wang, Applicability of eddy viscosity turbulence models in low specific speed centrifugal pump, IOP Conf. Ser.-Earth Environ. Sci. **15**, 062013 (2012).
20 F. R. Menter, Two-equation eddy-viscosity turbulence models for engineering applications, AIAA J. **32**, 1598 (1994).
21 R. Tao, R. Xiao, F. Wang, and W. Liu, Improving the cavitation inception performance of a reversible pump-turbine in pump mode by blade profile redesign: Design concept, method and applications, Renew. Energy **133**, 325 (2019).
22 C. Wang, F. Wang, C. Li, W. Chen, H. Wang, and L. Lu, Investigation on energy conversion instability of pump mode in hydro-pneumatic energy storage system, J. Energy Storage **53**, 105079 (2022).
23 F. Stern, R. V. Wilson, H. W. Coleman, and E. G. Paterson, Comprehensive approach to verification and validation of CFD simulations—Part 1: Methodology and procedures, J. Fluids Eng. **123**, 793 (2001).
24 C. J. Roy, Grid convergence error analysis for mixed-order numerical schemes, AIAA J. **41**, 595 (2003).
25 X. Gan, G. Pavesi, J. Pei, S. Yuan, W. Wang, and T. Yin, Parametric investigation and energy efficiency optimization of the curved inlet pipe with induced vane of an inline pump, Energy **240**, 122824 (2022).
26 S. Shen, Z. Qian, and B. Ji, Numerical analysis of mechanical energy dissipation for an axial-flow pump based on entropy generation theory, Energies **12**, 4162 (2019).
27 K. Kan, Q. Zhang, Z. Xu, Y. Zheng, Q. Gao, and L. Shen, Energy loss mechanism due to tip leakage flow of axial flow pump as turbine under various operating conditions, Energy **255**, 124532 (2022).
28 L. Ji, W. Li, W. Shi, H. Chang, and Z. Yang, Energy characteristics of mixed-flow pump under different tip clearances based on entropy production analysis, Energy **199**, 117447 (2020).
29 F. Kock, and H. Herwig, Local entropy production in turbulent shear flows: A high-Reynolds number model with wall functions, Int. J. Heat Mass Transfer **47**, 2205 (2004).
30 F. Kock, and H. Herwig, Entropy production calculation for turbulent shear flows and their implementation in cfd codes, Int. J. Heat Fluid Flow **26**, 672 (2005).
31 L. Duan, X. Wu, and Z. Ji, Application of entropy generation method for analyzing energy loss of cyclone separator, CIESC J. **65**, 583 (2014).
32 L. Duan, X. Wu, Z. Ji, and Q. Fang, Entropy generation analysis on cyclone separators with different exit pipe diameters and inlet dimensions, Chem. Eng. Sci. **138**, 622 (2015).
33 W. Li, E. Li, L. Ji, L. Zhou, W. Shi, and Y. Zhu, Mechanism and propagation characteristics of rotating stall in a mixed-flow pump, Renew. Energy **153**, 74 (2020).

不同流量工况下混流式喷水推进泵涡流所致能量损失

阚阚, 徐宇航, 徐辉, 冯建刚, 杨子轩

摘要 混流式喷水推进泵(M-FWPs)是高速船舶动力推进的核心部件. 当其在非最优工况下运行时, 流道中的不稳定流动会导致泵效率的下降. 本文通过数值模拟, 基于熵产理论研究了在不同工况下的能量损失机理. 对仿真数据的分析表明, 熵产率主要由湍流耗散产生. 通过比较速度梯度、涡度、湍动能以及湍动能耗散的相关性, 发现在非最优工况下, 由于叶轮进口入流角与叶片前缘进口角的不匹配, 会导致流动分离和大尺度漩涡等非稳定流动结构的发生. 这些非定常流动现象所导致的涡量和湍动能增强最终引起了熵增. 进一步检验拟涡能的输运发现涡生成项在非定常流动的产生过程中扮演了主要角色.